J|A|C|S
ARTICLES
Published on Web 03/04/2003

Single-Molecule Magnets: Two-Electron Reduced Version of a Mn_{12} Complex and Environmental Influences on the Magnetization Relaxation of $(PPh_4)_2[Mn_{12}O_{12}(O_2CCHCl_2)_{16}(H_2O)_4]$

Monica Soler,[†] Wolfgang Wernsdorfer,[‡] Khalil A. Abboud,[†] John C. Huffman,[§] Ernest R. Davidson,[§] David N. Hendrickson,[||] and George Christou*,[†]

Contribution from the Department of Chemistry, University of Florida, Gainesville, Florida 32611-7200, Laboratoire Louis Néel-CNRS, BP 166, 25 Avenue des Martyrs, 38042 Grenoble, Cedex 9, France, Department of Chemistry and Molecular Structure Center, Indiana University, Bloomington, Indiana 47405-7102, and Department of Chemistry, University of California at San Diego, La Jolla, California 92093-0358

Received August 9, 2002; E-mail: christou@chem.ufl.edu

Abstract: The complex $[Mn_{12}O_{12}(O_2CCHCl_2)_{16}(H_2O)_4]$ (**2**) in MeCN exhibits three quasi-reversible one-electron reduction processes at significantly higher potentials than $[Mn_{12}O_{12}(O_2CMe)_{16}(H_2O)_4]$ (**1**). This has allowed the two-electron reduced version of **2** to be generated and isolated. Reaction of **2** with one and two equivalents of PPh_4I led to isolation of $(PPh_4)[Mn_{12}O_{12}(O_2CCHCl_2)_{16}(H_2O)_4]$ (**3**) and $(PPh_4)_2[Mn_{12}O_{12}(O_2CCHCl_2)_{16}(H_2O)_4]$ (**4**), respectively. The latter represents a new isolated oxidation level of the Mn_{12} family of single-molecule magnets (SMMs). Crystallization from CH_2Cl_2/hexanes yields a mixture of two crystal forms, **4**·$4CH_2Cl_2$·H_2O (**4a**) and **4**·$6CH_2Cl_2$ (**4b**), both of which have been structurally characterized as triclinic and monoclinic, respectively. The molecular structures are very similar, with the added electrons localized on former Mn(III) ions to give a trapped-valence 2Mn(II), 6Mn(III), 4Mn(IV) oxidation state description. Dried solid analyzed as unsolvated **4**. ^1H NMR spectral data in CD_2Cl_2 confirm that **4** retains its solid-state structure in solution. Bulk DC magnetization data for dried **4** in the 1.80−4.00 K and 10−70 kG ranges were fit to give $S = 10$, $D = -0.275$ cm^{-1}, $g = 2.00$ and $|D|/g = 0.14$ cm^{-1}, where D is the axial zero-field splitting (anisotropy) parameter. Complexes **4a** and **4b** give resolvable frequency-dependent out-of-phase (χ_M'') signals in AC susceptibility studies resulting from the magnetization relaxation of SMMs. Relaxation rate vs T data to 1.8 K obtained from the χ_M'' vs temperature studies were supplemented with rate vs T data measured to lower temperatures via magnetization vs time decay data, and these were fit to the Arrhenius equation to give the effective barrier to relaxation (U_{eff}). The U_{eff} values are 18.5 and 30.3 K for **4a** and **4b**, respectively. A similar analysis for dried **4** using AC data gave $U_{eff} = 32$ K. Magnetization vs DC field sweeps on single crystals of **4a** and **4b** gave hysteresis loops containing steps due to quantum tunneling of magnetization (QTM). The step separations yielded $|D|/g$ values of 0.087 and 0.14 cm^{-1} for **4a** and **4b**, respectively, suggesting that the differences in U_{eff} are primarily caused by changes to D. The combined work demonstrates the sensitivity of the magnetic properties of these new $[Mn_{12}]^{2-}$ SMMs to subtle differences in their environment as determined by the precise packing, solvent molecules, and overall crystal symmetry (space group) and represents an important caveat to workers in the field.

Introduction

It was discovered in 1993 that single molecules of $[Mn_{12}O_{12}(O_2CMe)_{16}(H_2O)_4]$ (**1**) with a ground-state spin of $S = 10$ behave as superparamagnets and that they are thus magnets at very low temperatures.[1] There has since been great interest in trying to understand this new magnetic phenomenon of single-molecule magnetism and in finding other compounds that exhibit similar properties. Indeed, a few more manganese clusters,[2−4] as well as vanadium,[5] iron,[6] cobalt,[7] and nickel clusters[8] have been found to possess the necessary properties to function as single-molecule magnets (SMMs). However, of the SMMs known to date, the $[Mn_{12}O_{12}(O_2CR)_{16}(H_2O)_4]$ (R = various) family possesses the best structural and electronic properties for this

[†] University of Florida.
[‡] Laboratoire Louis Néel.
[§] Indiana University.
[||] University of California.

(1) (a) Sessoli, R.; Ysai, H.-L.; Schake, A. R.; Wang, S.; Vincent, J. B.; Folting, K.; Gatteschi, D.; Christou, G.; Hendrickson, D. N. *J. Am. Chem. Soc.* **1993**, *115*, 1804. (b) Sessoli, R.; Gatteschi, D.; Caneschi, A.; Novak, M. A. *Nature* **1993**, *356*, 141. (c) Christou, G.; Gatteschi, D.; Hendrickson, D. N.; Sessoli, R. *MRS Bull.* **2000**, *25*, 66.

(2) (a) Aubin, S. M. J.; Wemple, M. W.; Adams, D. M.; Tsai, H.-L.; Christou, G.; Hendrickson, D. N. *J. Am. Chem. Soc.* **1996**, 7746. (b) Andres, H.; Basler, R.; Gudel, H.-U.; Aromi, G.; Christou, G.; Buttner, H.; Ruffle, B. *J. Am. Chem. Soc.* **2000**, *122*, 12469. (c) Wernsdorfer, W.; Aliaga-Alcalde, N.; Hendrickson, D. N.; Christou, G. *Nature* **2002**, *416*, 406. (d) Aromi, G.; Bhaduri, S.; Artus, P.; Folting, K.: Christou, G. *Inorg. Chem.* **2002**, *41*, 805. (e) Aliaga-Alcalde, N.; Folting, K.; Hendrickson, D. N.; Christou, G. *Polyhedron* **2001**, *20*, 1273.

10.1021/ja021066s CCC: $25.00

phenomenon inasmuch as it displays single-molecule magnetism behavior at the highest temperatures.

The study of the physics of nanoscale magnetic particles has greatly benefited from the discovery of SMMs since the latter represented the availability, for the first time, of collections of magnetic "particles" with a single, sharply defined size, i.e., the molecular size. This allowed observation of quantum effects that had been predicted, but never before clearly seen, such as quantum tunneling of the magnetization (QTM).[9] This has led to a significant expansion of this field and contributed to the understanding of the consequences of taking magnetic materials to the limit of miniaturization, where quantum effects have to be taken into account.

Once it was known that single-molecule magnetism behavior requires a large ground-state spin and a magnetic anisotropy with a negative value of the zero-field splitting (ZFS) parameter D (i.e., Ising or easy-axis type anisotropy), efforts began to modify these molecules in a controlled fashion. This has been successful and has allowed the study of the effects of various modifications on the resulting magnetic properties, giving a better understanding of the structural and electronic factors that directly influence the latter. Work within the area of Mn_{12} coordination chemistry has led to the development of methods for major alteration of the chemical environment of the Mn_{12} core. It is possible, for example, to exchange the $MeCO_2^-$ ligands of $[Mn_{12}O_{12}(O_2CMe)_{16}(H_2O)_4]$ (**1**) for almost any other carboxylate group.[3a] This represented a big step forward because, among other things, it increased the solubility of these clusters in organic solvents and greatly altered their redox potentials; this resulted in a significant expansion of the chemistry of this family of molecules.[3a] One of the first results derived from the latter was the synthesis and isolation of salts containing the one-electron reduced species, $[Mn_{12}O_{12}(O_2CR)_{16}(H_2O)_4]^-$, which almost all have a $S = {}^{19}/_2$ ground state.[10] This permitted assessment of the structural and other consequences of changing the electron count in the Mn_{12} system as well as allowing study of the SMM phenomenon on a half-integer Mn_{12} derivative.[3a,b]

In this contribution, we report the extension of our work to the two-electron reduced Mn_{12} species. We describe the preparation and characterization of the prototypical $[Mn_{12}]^{2-}$ complex, $(PPh_4)_2[Mn_{12}O_{12}(O_2CCHCl_2)_{16}(H_2O)_4]$ (**4**), and show that it possesses an $S = 10$ ground state and retains the single-molecule magnetism properties of the Mn_{12} and $[Mn_{12}]^-$ analogues. Portions of this work have been briefly communicated.[11] In addition, recrystallization of **4** from CH_2Cl_2/hexanes gives two kinds of red-brown crystals with different morphologies, platelike $(PPh_4)_2[Mn_{12}O_{12}(O_2CCHCl_2)_{16}(H_2O)_4]\cdot 4CH_2Cl_2\cdot H_2O$ (**4**·$4CH_2Cl_2$·H_2O, or **4a**) and needlelike $(PPh_4)_2[Mn_{12}O_{12}(O_2CCHCl_2)_{16}(H_2O)_4]\cdot 6CH_2Cl_2$ (**4**·$6CH_2Cl_2$, or **4b**), both of which have been structurally characterized. The two forms have significantly different barriers to magnetization relaxation, emphasizing the influence of subtle environmental differences resulting from crystal packing (space group) symmetry and lattice solvent molecules on the resulting magnetic properties of SMMs.

Experimental Section

Compound Preparation. All chemical and solvents were used as received; all preparations and manipulations were performed under aerobic conditions. $[Mn_{12}O_{12}(O_2CMe)_{16}(H_2O)_4]\cdot 2MeCO_2H\cdot 4H_2O$ (**1**) was prepared as described elsewhere,[12] except that the reaction solution was not heated to 60 °C. $[Mn_{12}O_{12}(O_2CCHCl_2)_{16}(H_2O)_4]$ (**2**) was prepared as described elsewhere.[3c]

$(PPh_4)[Mn_{12}O_{12}(O_2CCHCl_2)_{16}(H_2O)_4]$ (3). Complex **2** (0.20 g, 0.067 mmol) was treated with a solution of PPh_4I (0.031 g, 0.067 mmol) in MeCN (50 mL). After 2 h, I_2 was removed by extraction into hexanes (6 × 25 mL), and the solution was rotoevaporated to dryness. The product was recrystallized from CH_2Cl_2/hexanes, and the microcrystalline product was filtered, washed with hexanes, and dried in vacuo. The yield was 65%. Elemental analysis: Calcd (Found) for **3**·1.6 C_6H_{14}: C, 22.85 (22.92); H, 1.94 (1.83).

$(PPh_4)_2[Mn_{12}O_{12}(O_2CCHCl_2)_{16}(H_2O)_4]$ (4). Complex **2** (0.40 g, 0.135 mmol) was treated with of PPh_4I (0.126 g, 0.270 mmol) in MeCN (50 mL). After 2 h, I_2 was removed by extraction into hexanes (6 × 25 mL), and the solution was rotoevaporated to dryness. The residue was recrystallized from CH_2Cl_2/hexanes, and the microcrystalline product was filtered, washed with hexanes, and dried in vacuo. The yield was 70%. Elemental analysis: Calcd (Found) for **4**: C, 26.06 (26.10); H, 1.78 (1.70). Samples for crystallography were grown slowly from CH_2Cl_2/hexanes layerings and were maintained in mother liquor to avoid solvent loss.

$(NPr^n_4)_2[Mn_{12}O_{12}(O_2CCHCl_2)_{16}(H_2O)_4]$ (4′). Complex **4′** was synthesized following the same procedure as above but using NPr^n_4I. Elemental analysis: Calcd (Found) for **4′**: C, 20.69 (20.40); H, 2.39 (2.57); N, 0.83 (0.80).

X-ray Crystallography. Crystalline samples of **4** usually comprise a mixture of two morphologies of which the platelike form (**4a**) is by far the majority species and the needlelike form (**4b**) is the minority species. Some samples appear essentially devoid of **4b**.

Data for **4a** and **4b** were collected at −80 °C on a Siemens SMART PLATFORM diffractometer at the University of Florida equipped with a CCD area detector and a graphite monochromator utilizing Mo Kα

(3) (a) Eppley, H. J.; Tsai, H.-L.; Vries, N.; Folting, K.; Christou, G.; Hendrickson, D. N. *J. Am. Chem. Soc.* **1995**, *117*, 301. (b) Aubin, S. M. J.; Sun, Z.; Pardi, L.; Krzystek, J.; Folting, K.; Brunel, L.-C.; Rheingold, A. L.; Christou, G.; Hendrickson, D. N. *Inorg. Chem.* **1999**, *38*, 5329. (c) Soler, M.; Artus, P.; Folting, K.; Huffman, J. C.; Hendrickson, D. N.; Christou, G. *Inorg. Chem.* **2001**, *40*, 4902. (d) Artus, P.; Boskovic. C.; Yoo, J.; Streib, W. E.; Brunel, L.-C.; Hendrickson, D. N.; Christou, G. *Inorg. Chem.* **2001**, *40*, 4199. (e) Boskovic. C.; Brechin, E. K.; Streib, W. E.; Folting, K.; Bollinger, J. C.; Hendrickson, D. N.; Christou, G. *J. Am. Chem. Soc.* **2002**, *124*, 3725.

(4) (a) Price, J. P.; Batten, S. R.; Moubaraki, B.; Murray, K. S. *Chem. Commun.* **2002**, 762. (b) Brechin, E. K.; Boskovic. C.; Wernsdorfer, W.; Yoo, J.; Yamaguchi, A.; Sañudo, E. C.; Concolino, T. R.; Rheingold, A. L.; Ishimoto, H.; Hendrickson, D. N.; Christou, G. *J. Am. Chem. Soc.* **2002**, *124*, 9710. (c) Brockman, J. T.; Huffman, J. C.; Christou, G. *Angew. Chem., Int. Ed.* **2002**, *41*, 2506. (d) Soler, M.; Rumberger, E.; Folting, K.; Hendrickson, D. N.; Christou, G. *Polyhedron* **2001**, *20*, 1365.

(5) Castro, S. L.; Sun, Z.; Grant, C. M.; Bollinger, J. C.; Hendrickson, D. N.; Christou, G. *J. Am. Chem. Soc.* **1998**, *120*, 2365.

(6) (a) Sangregorio, C.; Ohm, T.; Paulsen, C.; Sessoli, R.; Gatteschi, D. *Phys. Rev. Lett.* **1997**, *78*, 4645. (b) Oshio, H.; Hoshino, N.; Ito, T. *J. Am. Chem. Soc.* **2000**, *122*, 12602. (c) Barra, A. L.; Caneschi, A.; Cornia, A.; Fabrizi de Biani, F.; Gatteschi, D.; Sangregorio, C.; Sessoli, R.; Sorace, L. *J. Am. Chem. Soc.* **1999**, *121*, 5302.

(7) Yang, E.-C.; Hendrickson, D. N.; Wernsdorfer, W.; Nakano, M.; Zakharov, L. N.; Sommer, R. D.; Rheingold, A. L.; Ledezma-Gairaud, M.; Christou G. *J. Appl. Phys.* **2002**, *91*, 7382.

(8) Cadiou, C.; Murrie, M.; Paulsen, C.; Villar, V.; Wernsdorfer, W.; Winpenny, R. E. P. *Chem Commun.* **2001**, 2666.

(9) (a) Friedman, J. R.; Sarachik, M. P.; Tejada, J.; Ziolo, R. *Phys. Rev. Lett.* **1996**, *76* (20), 3830. (b) Thomas, L.; Lionti, L.; Ballou, R.; Gatteschi, D.; Sessoli, R.; Barbara, B. *Nature* **1996**, *383*, 145. (c) Tejada, J.; Ziolo, R. F.; Zhang, X. X. *Chem. Mater.* **1996**, *8*, 1784. (d) Aubin, S. M.; Gilley, N. R.; Pardi, L.; Krzystek, J.; Wemple, M. W.; Brunel, L. C.; Marple, M. B.; Christou, G.; Hendrickson, D. N. *J. Am. Chem. Soc.* **1998**, *120*, 4991. (e) Ruiz, D.; Sun, Z.; Albela, B.; Folting, K.; Christou, G.; Hendrickson, D. N. *Angew. Chem., Int. Ed.* **1998**, 300. (f) Hendrickson, D. N.; Christou, G.; Ishimoto, H.; Yoo, J.; Brechin, E. K.; Yamaguchi, A.; Rumberger, E. M.; Aubin, S. M. J.; Sun, Z.; Aromí, G. *Polyhedron* **2001**, *20*, 1479.

(10) Kuroda-Sowa, T.; Nakano, M.; Christou, G.; Hendrickson, D. N. *Polyhedron* **2001**, *20*, 1529.

(11) (a) Soler, M.; Chandra, S. K.; Ruiz, D.; Davidson, E. R.; Hendrickson, D. N.; Christou, G. *Chem. Commun.* **2000**, 2417−2418. (b) Soler, M.; Chandra, S. K.; Ruiz, D.; Huffman, J. C.; Hendrickson, D. N.; Christou, G. *Polyhedron* **2001**, *20*, 1279.

(12) Lis, T. *Acta Crystallogr.* **1980**, *B36*, 2042.

Table 1. Crystallographic Data for Complexes **4**·4CH_2Cl_2·H_2O (**4a**) at −80 and 22 °C and **4**·6CH_2Cl_2 (**4b**) at −80 °C

	4a	4a	4b
formula	$C_{84}H_{74}Cl_{40}Mn_{12}O_{49}P_2$	$C_{84}H_{74}Cl_{40}Mn_{12}O_{49}P_2$	$C_{86}H_{76}Cl_{44}Mn_{12}O_{48}P_2$
formula wt, g/mol[a]	4006.65	4006.65	4158.49
crystal system	triclinic	triclinic	monoclinic
space group	$P\bar{1}$	$P\bar{1}$	$P2/c$
a, Å	15.2645(5)	15.373(8)	18.713(2)
b, Å	22.0533(9)	22.127(11)	14.8714(8)
c, Å	22.2281(9)	22.273(12)	27.042(2)
α, deg	109.363(1)	108.768(12)	90
β, deg	93.650(1)	93.808(11)	97.767(2)
γ, deg	96.674(1)	97.151(12)	90
V, Å^3	6969.8(5)	7072(6)	7456.2(7)
Z	2	2	2
ρ_{calc}, Mg/m^3	1.909	1.882	1.852
μ, mm^{-1}	1.92	1.888	1.864
T, °C	−80	22	−80
λ, Å[b]	Mo Kα	Mo Kα	Mo Kα
final R indices	$R1 = 0.0449$	$R = 0.067$	$R1 = 0.0623$
$[I > 2\sigma(I)]$[c]	$wR2 = 0.1109$	$Rw = 0.058$	$wR2 = 0.1614$

[a] Including solvate molecules. [b] Graphite monochromator. [c] $R = R1 = \sum||F_o| - |F_c||/\sum|F_o|$. $wR2 = [\sum[w(F_o^2 - F_c^2)^2]/\sum[w(F_o^2)^2]]^{1/2}$, $w = 1/[\sigma^2(F_o^2) + (ap)^2 + bp]$, where $p = [\max(F_o^2, 0) + 2F_c^2]/3$. $R_w = [\sum w(|F_o| - |F_c|)^2/\sum w|F_o|^2]^{1/2}$ where $w = 1/\sigma^2(|F_o|)$.

radiation ($\lambda = 0.71073$ Å). Cell parameters were refined using up to 8192 reflections. A full sphere of data (1381 frames) was collected using the ω-scan method (0.3° frame width). The first 50 frames were remeasured at the end of data collection to monitor instrument and crystal stability (maximum correction on I was <1%). Absorption corrections by integration were applied on the basis of measured indexed crystal faces. The structures were solved by the direct methods in *SHELXTL5*, and refined using full-matrix least-squares. The non-H atoms were treated anisotropically, whereas the hydrogen atoms were calculated in ideal positions and were riding on their respective carbon atoms.

Complex **4**·4CH_2Cl_2·H_2O (**4a**) crystallizes in triclinic space group $P\bar{1}$, with the asymmetric unit consisting of the $[Mn_{12}]^{2-}$ anion, two PPh_4^+ cations, four CH_2Cl_2 molecules of crystallization, and a water molecule that has a 0.3 occupancy factor. There are several disorders in the Cl atoms of the ligands, and they were refined with dependent site occupation factors. One $CHCl_2CO_2^-$ ligand is disordered with a H_2O ligand, with the water coordinated to Mn(8) in some molecules, and to Mn(2) in the rest, and the carboxylate group correspondingly bridging Mn(1)/Mn(2) or Mn(1)/Mn(8), respectively. The water molecule in the lattice (O100) is hydrogen-bonded to the coordinated water (O19) on Mn(4). A total of 1784 parameters were refined in the final cycles of refinement on F^2 using 25355 reflections with $I > 2\sigma(I)$, giving $R1$ and $wR2$ of 4.49 and 11.09%, respectively.

Complex **4**·6CH_2Cl_2 (**4b**) crystallizes in the monoclinic space group $P2/c$, the asymmetric unit consisting of half a $[Mn_{12}]^{2-}$ anion lying on a C_2 symmetry axis, a PPh_4^+ cation, and three CH_2Cl_2 molecules of crystallization. Two CH_2Cl_2 molecules are located in general positions, one is disordered over a center of inversion, and one disordered over a C_2 symmetry axis. A total of 863 parameters were refined in the final cycles of refinement on F^2 using 8409 reflections with $I > 2\sigma(I)$ to yield R1 and wR2 of 6.23% and 16.14%, respectively.

Data were also collected for **4a** at Indiana University at room temperature using 10-s frames with an ω scan of 0.30°. Several methods were explored to keep the crystal wet with mother liquor while data were collected. The method finally used was to place a crystal and mother liquor in a Lindeman capillary, followed by centrifuging the tube until the crystal was wedged securely. Despite this, the crystal appeared to move significantly during the first set of frames, and near the end of the data collection. Since multiply redundant data had been collected, the initial and final frame sets were discarded for the data analysis. An absorption correction was performed using the SADABS program supplied by Bruker AXS. The structure was solved using SHELXTL and Fourier techniques, and refined on F by full-matrix least-squares cycles.

The final values of discrepancy indices $R(R_w)$ or R1(wR2) are listed in Table 1.

Physical Measurements. Direct current (DC) and alternating current (AC) magnetic susceptibility studies were performed at the University of Florida on a Quantum Design MPMS-XL SQUID susceptometer equipped with a 7 T magnet and operating in the 1.8−400 K range. Pascal's constants were used to estimate the diamagnetic corrections for the compounds. Samples were embedded in solid eicosane to prevent torquing. Magnetization vs field and temperature data were fit using the program MAGNET, and contour plots were obtained using the program GRID, both written at Indiana University by E.R.D. Elemental analyses were carried out at the University of Florida. Electrochemical studies were performed under argon using a BAS model CV-50W voltammetric analyzer and a standard three-electrode assembly (glassy carbon working, Pt wire auxiliary, and $Ag/AgNO_3$ reference) with 0.1 M $NBu^n_4PF_6$ as supporting electrolyte. No IR compensation was employed. Quoted potentials are vs the ferrocene/ferrocenium couple, used as an internal standard. The scan rates for cyclic voltammetry (CV) and differential pulse voltammetry (DPV) were 100 and 20 mV/s, respectively. Distilled solvents were employed, and the concentrations of the complexes were approximately 1 mM. ^{1}H NMR spectra were obtained at 300 MHz on a Varian XL-300 spectrometer, using protio-solvent signals as internal references. Infrared spectra were recorded on KBr pellets using a Nicolet 510P FTIR spectrophotometer. Low-temperature (<1.8 K) hysteresis loop and DC relaxation measurements were performed at Grenoble using an array of micro-SQUIDs.[13] The high sensitivity of this magnetometer allows the study of single crystals of SMMs of the order of 10−500 μm. The field can be applied in any direction by separately driving three orthogonal coils.

Results

Syntheses. One of the first reactivity properties of $[Mn_{12}O_{12}(O_2CMe)_{16}(H_2O)_4]$ (**1**) to be established was its ability to undergo carboxylate substitution reactions.[3a] The treatment of **1** with an excess of RCO_2H in two cycles led to the clean conversion to $[Mn_{12}O_{12}(O_2CR)_{16}(H_2O)_4]$ (eq 1).

$$[Mn_{12}(O_2CMe)_{16}(H_2O)_4] + 16\ RCO_2H \rightarrow [Mn_{12}O_{12}(O_2CR)_{16}(H_2O)_4] + 16\ MeCO_2H \quad (1)$$

Repeated treatment is required because the ligand substitution is an equilibrium that must be driven to completion. This reaction has allowed a number of Mn_{12} complexes to be obtained

(13) Wernsdorfer, W. *Adv. Chem. Phys.* **2001**, *118*, 99.

that differ in their carboxylate ligation, and this method was used to prepare the dichloroacetate derivative in the present work.

In a previous report, we showed that the $[Mn_{12}O_{12}(O_2CR)_{16}(H_2O)_4]$ complexes have a rich redox chemistry involving both multiple oxidations and reductions and that the potentials of these processes are quite sensitive to the identity of the carboxylate groups.[3a] One oxidation process and two reduction processes were observed for the R = Me complex **1**, but only the first reduction at 0.19 V vs Fc/Fc^+ appeared to be quasi-reversible by the normal electrochemical criteria.[1a,3a,14,] We subsequently demonstrated that the one-electron reduced complexes could be generated in bulk by reduction with I^- in CH_2Cl_2 (eq 2), and isolated and structurally characterized the reduced

$$[Mn_{12}O_{12}(O_2CR)_{16}(H_2O)_4] + I^- \rightarrow [Mn_{12}O_{12}(O_2CR)_{16}(H_2O)_4]^- + 0.5I_2 \quad (2)$$

$[Mn_{12}]^-$ derivative as its PPh_4^+ salt from the reaction of the neutral complex $[Mn_{12}O_{12}(O_2CEt)_{16}(H_2O)_4]$ with PPh_4I.[3a] The introduction of more electron-withdrawing substituents into the carboxylate groups of the Mn_{12} complexes suggested the possibility of obtaining two-electron reduced Mn_{12} complexes, and this proved to be the case. A new family of two-electron reduced Mn_{12} complexes has now been synthesized and characterized. The prototype of this family was $(PPh_4)_2[Mn_{12}O_{12}(O_2CCHCl_2)_{16}(H_2O)_4]$ (**4**) synthesized from $[Mn_{12}O_{12}(O_2CCHCl_2)_{16}(H_2O)_4]$ (**2**).

The cyclic voltammogram (CV) and differential pulse voltammogram (DPV) for complex **2** are shown in Figure 1. It displays three reduction processes, with an anodic shift of the reduction potentials compared with **1** as expected from the electron-withdrawing substituents. In addition, both the first and second reductions appear reversible by electrochemical criteria (CV peak separations, I_f vs I_r, DPV peak sharpness). Even a third reduction appears reversible. The anodic shifts make the second reduction accessible with I^-, the reducing agent used for one-electron reductions. Therefore, $[Mn_{12}O_{12}(O_2CCHCl_2)_{16}(H_2O)_4]$ (**2**) was treated with two equivalents of PPh_4I in MeCN, and the formation of I_2 was confirmed by its extraction into a hexane phase. Removal of MeCN in vacuo and recrystallization from CH_2Cl_2/hexanes gave black crystalline material in good yield (≥60%) and analytical purity, and this proved to be the desired two-electron reduced complex **4** (eq 3).

$$[Mn_{12}O_{12}(O_2CR)_{16}(H_2O)_4] + 2\,I^- \rightarrow [Mn_{12}O_{12}(O_2CR)_{16}(H_2O)_4]^{2-} + I_2 \quad (3)$$

The PPh_4^+ cations provide salts that are highly crystalline while retaining sufficient solubility for spectroscopic studies. However, the reaction of eq 3 can be readily extended to a variety of other cations.

Description of Structures. Two types of crystals have been identified from the recrystallization of complex **4** in CH_2Cl_2/hexanes; the majority by far is platelike (**4a**) and the minority is needlelike (**4b**). In some crystallizations, only **4a** is apparent. Color PovRay plots of the anions of complex **4a** and **4b** are presented in Figures 2 and 3. Stereoviews of the packing in each crystal are provided as Supporting Information. A comparison of pertinent interatomic distances and angles is given in Table 2.

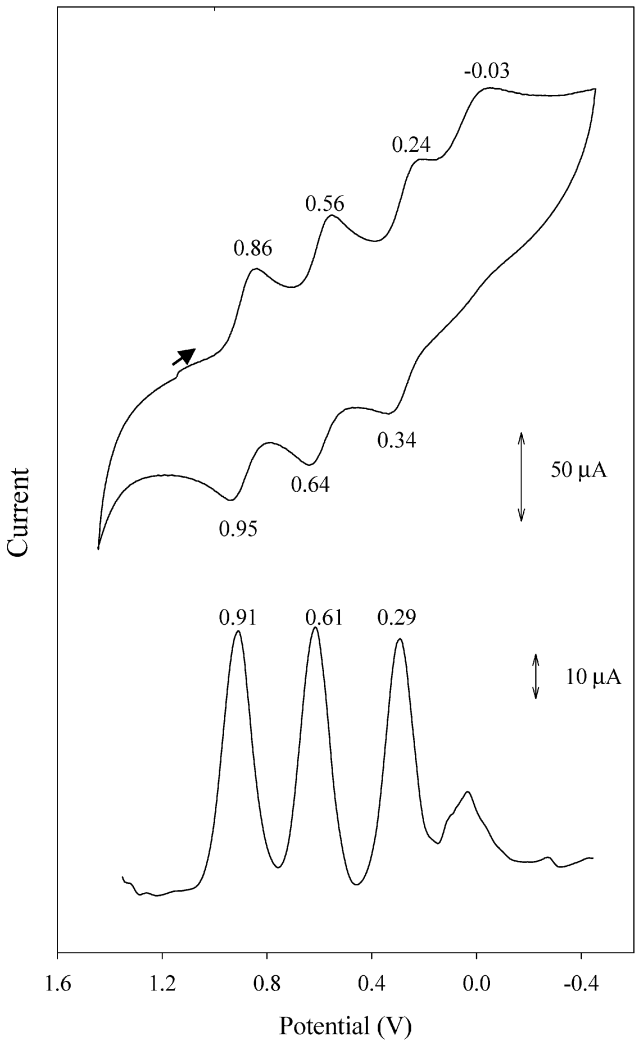

Figure 1. Cyclic voltammogram at 100 mV s^{-1} (top) and differential pulse voltammogram (bottom) for complex **2** in MeCN containing 0.1 M $NBu^n_4PF_6$ as supporting electrolyte. The indicated potentials are vs Fc/Fc^+.

Complex **4a** crystallizes in a triclinic space group $P\bar{1}$, with two $[Mn_{12}]^{2-}$ anions in the unit cell. The anion consists of a central $[Mn_4O_4]$ cubane surrounded by a nonplanar ring of eight Mn atoms that are bridged and connected to the cubane by eight μ_3-O^{2-} ions (Figure 2). Peripheral ligation is by 16 bridging $CHCl_2CO_2^-$ and four terminal H_2O groups. All Mn are six-coordinate, with near-octahedral geometries. In the neutral Mn_{12} molecules, the four central cubane Mn are Mn^{IV}, and the eight ring Mn atoms are Mn^{III}. When reduced by one electron to give the $[Mn_{12}]^-$ anion, the added electron is localized on a ring (formerly Mn^{III}) Mn atom making it Mn^{II}. The $[Mn_{12}]^-$ anion is thus trapped-valence Mn^{II}, $7Mn^{III}$, $4Mn^{IV}$. Therefore, the structural parameters for **4a** were closely inspected to identify where the added electrons were situated. The structure of the central cubane is essentially superimposable with those for the Mn_{12} and $[Mn_{12}]^-$ analogues, and thus these Mn are still Mn^{IV}. For the ring Mn atoms, the Mn−O bond lengths unequivocally establish that the added electrons have gone one each on two formerly Mn^{III} atoms and converted them to Mn^{II}. These Mn atoms are Mn(4) and Mn(8). Qualitatively, this is evident in

(14) Schake, A. R.; Tsai, H.-L.; Vries, N.; Webb, R. J.; Folting, K.; Hendrickson, D. N.; Christou, G. *J. Chem. Soc., Chem. Commun.* **1992**, 181.

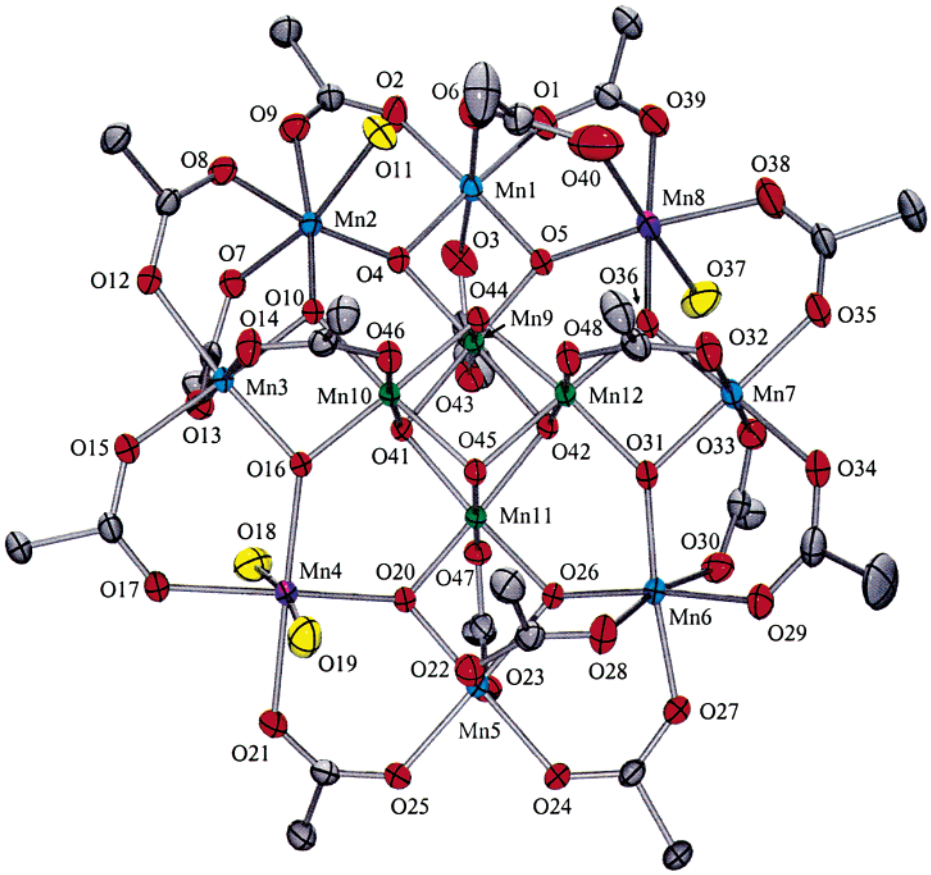

Figure 2. Color ORTEP PovRay plot of the anion of $(PPh_4)_2[Mn_{12}O_{12}(O_2CCHCl_2)_{16}(H_2O)_4]\cdot 4CH_2Cl_2\cdot H_2O$ (**4a**) with thermal ellipsoids at the 50% probability level. For clarity, the Cl atoms are omitted. Mn^{IV} green; Mn^{III} blue; Mn^{II} purple; O red; H_2O yellow; C gray.

the longer Mn−O bond distances at the latter two Mn, and the appearance of Jahn−Teller axial elongations at the other six ring Mn atoms, as expected for high-spin Mn^{III} (d^4) in near-octahedral geometry (Table 2). Quantitatively, the individual Mn oxidation levels were determined by a bond valence sum (BVS) calculation whose results are listed in Table 3. This clearly establishes that Mn(4) and Mn(8) are Mn^{II}. Thus, the $[Mn_{12}]^{2-}$ anion is a trapped-valence $2Mn^{II}$, $6Mn^{III}$, $4Mn^{IV}$ species. As for $[Mn_{12}]^{-}$, we assign this preferential reduction of a Mn^{III} rather than a Mn^{IV} as due to the strain that would be introduced into the relatively rigid central cubane if a Mn^{IV} were to be reduced to a JT distorted Mn^{III}. To answer the question whether the trapped-valence nature of **4a** is a consequence of the low-temperature employed for the crystal structure determination, data were also collected for **4a** at 22 °C. A comparison of selected distances for the two structures at −80 and 22 °C is available as Supporting Information, and it is clear that the added electrons are still trapped in the solid state at 22 °C. This was confirmed by BVS calculations.

Owing to a static disorder between one carboxylate group and an adjacent water molecule, the structure is a mixture of two isomers, the 1:1:2 form (70%) and the 2:2 form (30%), referring to the distribution of the four H_2O molecules. Form 1:1:2 has the carboxylate bridging Mn(1) and Mn(8) with the H_2O molecule on Mn(2), and the 2:2 form has the carboxylate bridging Mn(1) and Mn(2) with the water molecule on Mn(8). The other three waters are always located on the Mn^{II} ions, two on Mn(4) and the third on Mn(8).

Complex **4b** crystallizes in the monoclinic space group *P*2/c, and the structure (Figure 3) of the $[Mn_{12}]^{2-}$ anion is overall very similar to that for **4a**. There is a crystallographic C_2 axis passing through Mn(1) and Mn(7). The Mn oxidation states were again assigned by inspection of the bond distances (Table 2) and by BVS calculations (not shown), and the Mn^{II} atoms are Mn(4) and Mn(4a). No disorder in the H_2O positions was seen in this structure, unlike that of **4a**; the four H_2O molecules are bound in a 2:2 fashion to the Mn^{II} atoms. It is interesting to note that in both structures, the Mn^{II} centers are disposed trans. There seems no reason there should be a strong preference for this arrangement rather than cis, for example, Mn(2) and Mn(4) in Figure 2 rather than Mn(4) and Mn(8). It is possible that such a cis disposition may be seen in a future X-ray structure of a $[Mn_{12}]^{2-}$ complex. Note also that there is, however, a preference for the H_2O molecules to bind to the Mn^{II} centers, or rather a preference by the Mn^{III} centers for the anionic carboxylate ligands, as expected from simple charge considerations.

^{1}H NMR Spectroscopy. An ^{1}H NMR spectroscopic study of complexes **2**, **3**, and **4** was carried out to probe their structure and stability in solution. True solubility in organic solvents is a major advantage of SMMs over classical magnetic nanoparticles, but only if their structure (and thus their magnetic properties) remains unchanged on dissolution. The ^{1}H NMR spectrum of a CD_2Cl_2 solution of neutral $[Mn_{12}O_{12}(O_2CCHCl_2)_{16}(H_2O)_4]$ (**2**) exhibits three peaks with a 1:1:2 integration ratio (Figure 4, bottom), indicating that there are only three magnetically distinguishable types of dichloroacetate ligands. This

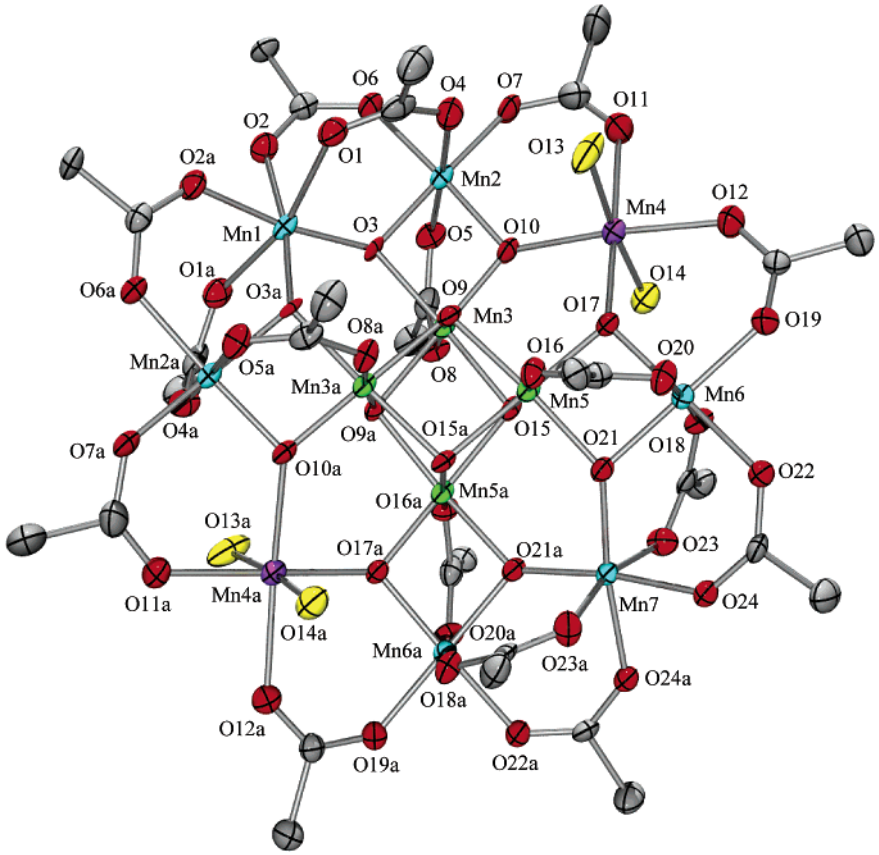

Figure 3. Color ORTEP PovRay plot of the anion of $(PPh_4)_2[Mn_{12}O_{12}(O_2CCHCl_2)_{16}(H_2O)_4]\cdot 6CH_2Cl_2$ (**4b**) with thermal ellipsoids at the 50% probability level. For clarity, the Cl atoms have been omitted. Mn^{IV} green; Mn^{III} blue; Mn^{II} purple; O red; H_2O yellow; C gray.

Table 2. Comparison of Selected Bond Distances (Å) and Angles (deg) for Complexes $4\cdot 4CH_2Cl_2\cdot H_2O$ (**4a**) and $4\cdot 6CH_2Cl_2$ (**4b**)

parameter[a]	4a	4b
$Mn^{IV}-O_c$ (ax)	1.886(2)−1.898(2)	1.877(4)−1.894(4)
$Mn^{IV}-O_c$ (eq)	1900(2)−1.962(2)	1.915(4)−1.953(4)
$Mn^{IV}-O_r$	1.826(2)−1.899(2)	1.824(4)−1.888(4)
$Mn^{IV}-O_{ax}$	1.952(2)−1.973(2)	1.945(8)
$Mn^{IIIb}-O_r$	1.849(2)−1.920(2)	1.853(4)−1.901(4)
$Mn^{IIIc}-O_r$	1.859(2)−1.879(2)	1.864(4)−1.875(4)
$Mn^{IIIb}-O_{eq}$	1.944(2)−1.988(3)	1.939(4)−1.978(4)
$Mn^{IIIc}-O_{eq}$	1.956(2)−1.979(2)	1.968(4)−1.971(4)
$Mn^{IIIb}-O_{ax}$	2.202(2)−2.252(2)	2.219(5)−2.258(4)
$Mn^{IIIb}-O_{ax}$*	2.137(3)−2.166(3)	–
$Mn^{IIIc}-O_{ax}$	2.121(2)−2.148(3)	2.165(4)−2.201(4)
$Mn^{IIIc}-O_w$	2.241(7)	–
$Mn^{II}-O_r$	2.101(2)−2.108(2)	2.111(4)−2.131(4)
$Mn^{II}-O_{eq}$	2.149(2)−2.179(3)	2.172(4)−2.173(5)
$Mn^{II}-O_{ax}$	2.165(4)	–
$Mn^{II}-O_w$	2.209(3)−2.229(3)	2.180(5)−2.186(5)

parameter[a]	4a	4b
$O_r-Mn^{IV}-O_r$	84.20(9)−85.06(10)	84.38(17)−84.28(17)
$O_r-Mn^{IIIb}-O_r$	83.07(9)−83.59(9)	83.14(16)−83.51(17)
$O_r-Mn^{IIIc}-O_r$	94.34(10)−94.37(10)	94.1(2)−94.5(2)
$O_r-Mn^{II}-O_r$	91.95(8)−92.45(9)	92.67(15)

[a] O_c = cubane O^{2-}, O_r = ring O^{2-}, O_{ax} = axial carboxylate, O_{eq} = equatorial carboxylate, O_w = water. *Involves the carboxylate/water disorder at Mn(1). [b] Mn^{IIIb} atoms: Mn(1, 3, 5 and 7) in **4a** and Mn(2 and 6) in **4b**. [c] Mn^{IIIc} atoms: Mn(2 and 6) in **4a** and Mn(1 and 7) in **4b**.

pattern has been seen previously for other neutral Mn_{12} complexes,[3a] and it reflects effective D_{2d} solution symmetry. In the solid state, the neutral Mn_{12} complexes have anything up to virtual D_2 or S_4 symmetry, depending on the exact relative positions of the carboxylate and H_2O ligands. In solution,

Table 3. Bond Valence Sums[a] for $4\cdot 4CH_2Cl_2\cdot H_2O$ (**4a**)

atom	Mn^{II}	Mn^{III}	Mn^{IV}
Mn(1)	3.2838	<u>3.0036</u>	3.1533
Mn(2)	3.3613	<u>3.0745</u>	3.2278
Mn(3)	3.2474	<u>2.9703</u>	3.1183
Mn(4)	<u>2.0868</u>	1.9087	2.0039
Mn(5)	3.1833	<u>2.9117</u>	3.0568
Mn(6)	3.3291	<u>3.0450</u>	3.1968
Mn(7)	3.2382	<u>2.9619</u>	3.1096
Mn(8)	<u>2.0793</u>	1.9019	1.9967
Mn(9)	4.0762	3.7284	<u>3.9143</u>
Mn(10)	4.1626	3.8074	<u>3.9972</u>
Mn(11)	4.1221	3.7704	<u>3.9583</u>
Mn(12)	4.1410	3.7876	<u>3.9765</u>

[a] The underlined value is the one closest to the charge for which it was calculated. The oxidation state of a particular atom can be taken as the nearest whole number to the underlined value.

effective D_2 or S_4 symmetry would give four types of carboxylate ligands, two axial and two equatorial, and thus four NMR resonances in a 1:1:1:1 ratio. However, a fluxional process that is fast on the ^1H NMR time scale has previously[3d] been identified in which fast exchange between the H_2O ligands and one type of axial carboxylate ligand takes place, and this introduces dihedral mirror planes which make all the equatorial carboxylate groups equivalent. The effective solution symmetry is thus D_{2d}, and three NMR resonances are seen in a 1:1:2 (ax:ax:eq) ratio. The peak corresponding to the equatorial (eq) carboxylate groups appears at δ = 11.7 ppm, close to the diamagnetic region, while the two axial peaks are located much further downfield. The peak at δ = 24.5 ppm is from the four dichloroacetate groups that bridge the four $Mn^{III}\cdots Mn^{IV}$ pairs, while the peak at δ = 40.8 ppm is from the four axial

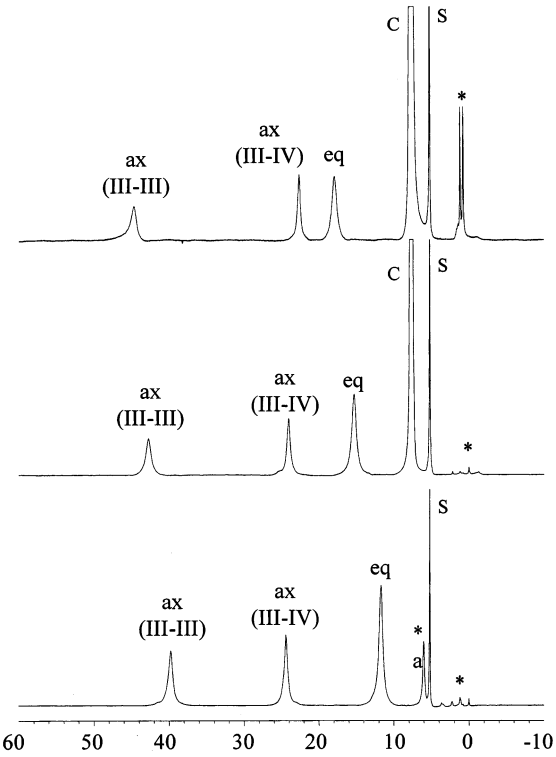

Figure 4. ^{1}H NMR (300 MHz) spectra at ~23 °C in CD_2Cl_2 solution of **2** (bottom), **3** (middle) and **4** (top): * are solvent impurities; s is solvent protio-impurity.

Table 4. Solution ^{1}H NMR Spectral Data for $[Mn_{12}O_{12}(O_2CR)_{16}(H_2O)_4]^z$ Complexes

compound	peak[a]	assignment[b]	T_1[c]
$z = 0$, R = Me (**1**)[d]	13.9	ax (III−IV)	5.7
	41.8	eq (III−III)	3.4
	48.2	ax (III−III)	3.3
$z = 0$, R = $CHCl_2$ (**2**)[e]	11.7	eq (III−III)	3.0
	24.5	ax (III−IV)	5.2
	40.8	ax (III−III)	3.0
$z = 1-$, R = $CHCl_2$ (**3**)[e]	15.5	eq (III−III)	2.6
	24.0	ax (III−IV)	4.5
	41.7	ax (III−III)	2.6
$z = 2-$, R = $CHCl_2$ (**4**)[e]	18.0	eq (III−III)	2.0
	22.7	ax (III−IV)	4.0
	44.4	ax (III−III)	2.0

[a] ppm, at ~23 °C. [b] ax = axial, eq = equatorial; III−III and III−IV refer to the ligand bridging a $Mn^{III}Mn^{III}$ and $Mn^{III}Mn^{IV}$ pair, respectively. [c] ms. [d] In CD_3CN. [e] In CD_2Cl_2.

dichloroacetate groups bridging the four $Mn^{III}\cdots Mn^{III}$ pairs. The assignments are collected in Table 4. They were based on spin−lattice relaxation times (T_1), measured using the inversion recovery method (in general, the longitudinal relaxation time is related to the distance of a nucleus from the paramagnetic center), and comparisons with the corresponding spectrum of $[Mn_{12}O_{12}(O_2CMe)_{16}(H_2O)_4]$ (**1**).[3a]

The spectra of the $[Mn_{12}]^-$ and $[Mn_{12}]^{2-}$ versions of **2**, i.e., complexes **3** and **4**, respectively, are also shown in Figure 4 (middle and top). Apart from the presence of the PPh_4^+ signals in the spectra of **3** and **4**, the three spectra display the same profile of only three resonances in a 1:1:2 ratio, with only relatively small changes in their chemical shifts. This indicates that the $[Mn_{12}]^-$ and $[Mn_{12}]^{2-}$ complexes also display effective D_{2d} symmetry in solution, which is consistent with detrapping on the ^{1}H NMR time scale of the added electrons among the outer ring of Mn ions, and this detrapping is likely coupled to the H_2O/RCO_2^- ligand fluxionality mentioned above. Chemical shifts and T_1 times for **1**, **2**, **3**, and **4** are listed in Table 4.

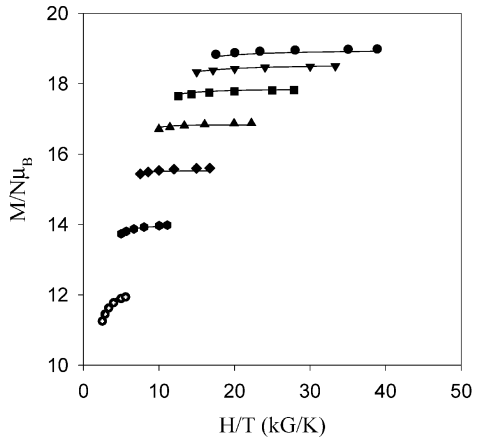

Figure 5. Plot of $M/N\mu_B$ vs H/T for complex **4** at the indicated applied fields. The solid lines are the fit of the data; see the text for the fit parameters.

Magnetochemistry

Magnetochemical studies were performed using both DC and AC methods. There are three forms of **4**, as described above, and all were studied as appropriate to characterize the complex and determine the influence on the observed magnetic properties of the sample's crystal form and solvation level. The three forms are dried powder of **4**, triclinic plates of $\mathbf{4}\cdot 4CH_2Cl_2\cdot H_2O$ (**4a**), and monoclinic needles of $\mathbf{4}\cdot 6CH_2Cl_2$ (**4b**).

DC Magnetic Susceptibility Studies. Variable-temperature DC magnetic susceptibility (χ_M) data were collected on complex **4** in the 2.00−300 K range in a 10 kG (1 T) magnetic field. The $\chi_M T$ value slowly increases from 21.00 cm^3 K mol^{-1} at 300 K to a maximum of 45.35 cm^3 K mol^{-1} at 15.0 K and then decreases rapidly at lower temperatures (see Supporting Information). The maximum value indicates a high ground-state spin (S) value for **4**; the 300 K value is less than that expected for noninteracting metal ions in **4**, indicating the presence of intramolecular exchange interactions.

Since the size of the $[Mn_{12}]^{2-}$ cluster is too great to allow determination of the many individual pairwise exchange parameters between Mn ions, we focused our efforts on determining the ground state of **4**. Thus, magnetization (M) data were collected in the 10−70 kG and 1.80−4.00 K ranges. The data are plotted as reduced magnetization ($M/N\mu_B$) vs H/T in Figure 5, where N is Avogadro's number and μ_B is the Bohr magneton. For a system occupying only the ground state and experiencing no zero-field splitting (ZFS), the various isofield lines would be superimposed and $M/N\mu_B$ would saturate at a value of gS. The nonsuperimposition of the isofield lines clearly indicates the presence of ZFS. The data were fit using MAGNET,[15] which assumes only the ground state is populated at these temperatures and is based on the method described elsewhere involving diagonalization of the spin Hamiltonian matrix, including axial ZFS ($D\hat{S}_z^2$) and Zeeman interactions, and incorporating a full powder average.[16] The best fit is shown as the solid lines in Figure 5, and the fitting parameters were $S = 10$, $D = -0.27$

(15) (a) Davidson, E. R. *MAGNET*; Indiana University: Bloomington, IN. (b) Davidson, E. R. *GRID*; Indiana University: Bloomington, IN.
(16) Yoo, J.; Yamaguchi, A.; Nakano, M.; Krzystek, J.; Streib, W. E.; Brunel, L.-C.; Ishimoto, H.; Christou, G.; Hendrickson, D. N. *Inorg. Chem.* **2001**, *40*, 4604.

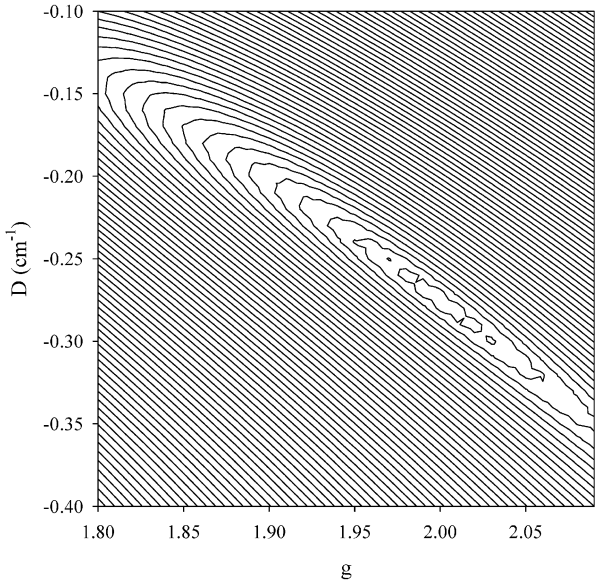

Figure 6. Two-dimensional contour plot of the error surface for the D vs g fit for complex **4**.

$cm^{-1} = -0.39$ K and $g = 2.00$. To confirm that the obtained minimum was the true global minimum, a root-mean-square D vs g error surface for the fit was generated with the program GRID,[15] which calculates the relative difference between the experimental $M/N\mu_B$ data and those calculated for various combinations of D and g. This is shown as a contour plot in Figure 6 for the $D = -0.10$ to -0.40 cm^{-1} and $g = 1.80-2.10$ ranges. Only one fitting minimum is observed, but it is a rather soft minimum with the contour describing the region of minimum error encompassing $D \approx -0.255$ to -0.295 cm^{-1} and $g \approx 1.98-2.02$, giving fitting parameters of $D = -0.275 \pm 0.020$ cm^{-1} and $g = 2.00 \pm 0.02$, and a $|D|/g$ ratio of 0.14 ± 0.01 cm^{-1}.

For comparison, similar variable-temperature and -field data magnetization data were also collected for the neutral and one-electron reduced analogues with the same carboxylate group, i.e., **2** and **3**, respectively. The results are shown in Figure 7, and the fitting parameters compared in Table 5.

The ground-state spin of **4** is thus similar to the $S = 10$ and $^{19}/_2$ values for the Mn_{12} (**2**) and $[Mn_{12}]^-$ (**3**) complexes, respectively. However, the anisotropy, as reflected in the absolute value of D, decreases as the $[Mn_{12}]$ gets progressively reduced. This is as expected: the main source of the molecular anisotropy is the single-ion anisotropies of the Mn^{III} ions, which are Jahn−Teller distorted; Mn^{II} and Mn^{IV} are fairly isotropic ions. Since the added electrons on reduction are localized on formerly Mn^{III} ions converting them to Mn^{II}, reduction leads to a decrease in the number of Mn^{III} ions and a concomitant decrease in the molecular anisotropy. The D values in Table 5 are approximate numbers, and thus are most useful for relative comparisons, because the fitting model assumes axial symmetry and these complexes are all crystallographically rhombic. It is interesting that the spin value does not change on two-electron reduction compared with Mn_{12}. In this sense, the complexes act as a "spin buffer", picking up electrons with little or no change to the S value.

The $S = 10$ value of the $[Mn_{12}]^{2-}$ complexes, together with an anisotropy that has been decreased but is still reasonably large, implies that they might still function as SMMs, i.e still possess a sufficiently large barrier to magnetization reversal that they display slow magnetization relaxation (reorientation) rates. The upper limit for this barrier (U) can be calculated as $U = S^2|D|$ for integer spins and $U = (S^2 - 1/4)|D|$ for half-integer spins;[1−3,17] these values of U for **2**−**4** are included in Table 5. AC susceptibility studies were therefore performed.

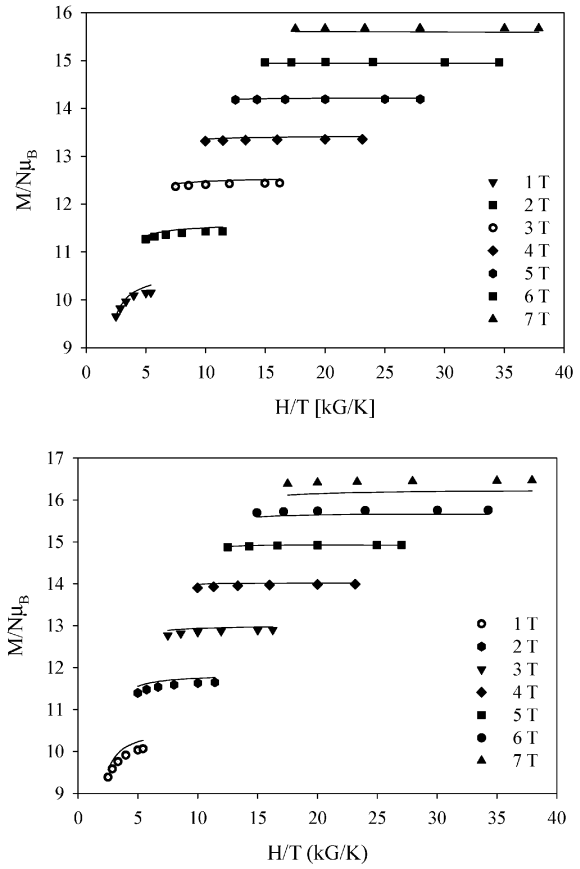

Figure 7. Plot of $M/N\mu_B$ vs H/T for complexes **2** (top) and **3** (bottom) at the indicated applied fields. The solid lines are the fits of the data; see Table 5 for the fit parameters.

Table 5. $M/N\mu_B$ vs H/T Fit Data for Dried $[Mn_{12}O_{12}(O_2CCHCl_2)_{16}(H_2O)_4]^{0,-,2-}$ Complexes

	Mn_{12} (**2**)	$[Mn_{12}]^-$ (**3**)	$[Mn_{12}]^{2-}$ (**4**)
S	10	19/2	10
g	1.86	1.87	2.00
D, cm^{-1}	−0.45	−0.34	−0.27
D, K	−0.65	−0.49	−0.39
U, K	65	44	39

AC Magnetic Susceptibility Studies. In an AC susceptibility experiment, a weak field (typically 1−5 G) oscillating at a particular frequency (ν) is applied to a sample to probe the dynamics of the magnetization (magnetic moment) relaxation. An out-of-phase AC susceptibility signal (χ_M'') is observed when the rate at which the magnetization of a molecule relaxes is close to the operating frequency of the AC field. At low enough temperature, where the thermal energy is lower than the barrier for relaxation, the magnetization of the molecule cannot relax

(17) (a) Kuroda-Sowa, T.; Lam, M.; Rheingold, A. L.; Frommen, C.; Reiff, W. M.; Nakano, M.; Yoo, J.; Maniero, A. L.; Brunel, L.-C.; Christou, G.; Hendrickson, D. N. *Inorg. Chem.* **2001**, 6469. (b) Kuroda-Sowa, T.; Nakano, M.; Christou, G.; Hendrickson, D. N. *Polyhedron* **2001**, *20*, 1529.

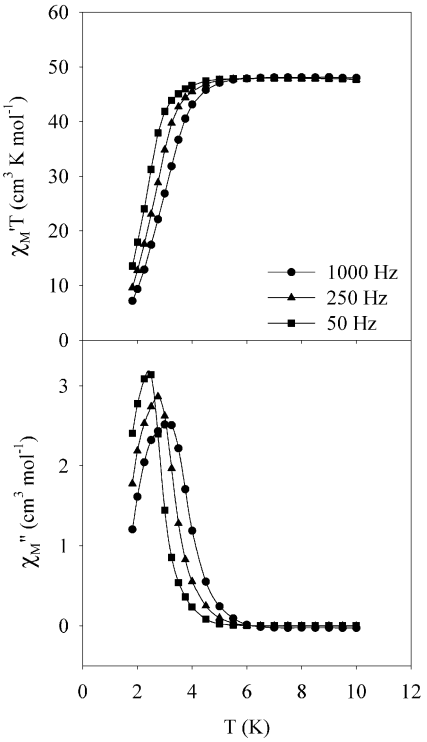

Figure 8. In-phase (χ_M') and out-of-phase (χ_M'') AC susceptibility signals for dried complex **4** at the indicated frequencies.

fast enough to keep in-phase with the oscillating field. Therefore, the molecule will exhibit a frequency-dependent χ_M'' signal indicative of slow magnetization relaxation. Frequency-dependent χ_M'' signals are an important indicator of SMMs. Further, AC magnetic susceptibility data can be used not only to determine whether a molecule functions as a SMM but also to obtain the spin ground state (S) and the effective energy barrier U_{eff} for the magnetization relaxation.

AC magnetic susceptibility studies at zero DC field and 3.5 G AC field were carried out to probe the magnetization relaxation dynamics of complex **4** at low temperatures (1.8−10 K). Figure 8 shows the in-phase (χ_M', plotted as $\chi_M'T$ vs T (top)) and the out-of-phase (χ_M'' vs T (bottom)) components of the AC magnetic susceptibility. If it is assumed that only the ground state of complex **4** is thermally populated in the 1.8−10 K range, the $\chi_M'T$ plateau at ∼48 cm^3 K mol^{-1} indicates a $S = 10$ ground state with $g \approx 1.9$. In the χ_M'' plot, a frequency-dependent χ_M'' peak is observed in the range 2−4 K at 50−1000 Hz. This establishes that complex **4** is a SMM.

The 2−4 K range of the χ_M'' peak is lower than the 4−6 K and 6−8 K ranges for $[Mn_{12}]^-$ and Mn_{12}, respectively. This is summarized for the three oxidation states in Figure 9, and reflects a decreasing barrier to magnetization relaxation with reduction.

If the χ_M'' signal for dried **4** at 1000 Hz in Figures 8 and 9 is inspected carefully, it is apparent that it does not have a symmetric line shape but instead appears to be two separate, unresolved signals. Since we knew that solvent is lost on vacuum-drying, we repeated these studies with a crystalline solid that had been kept wet with mother liquor, hoping for better resolution. Indeed, this now resulted in resolution of two χ_M'' signals, shown in Figure 10 for a 500-Hz frequency, and these were readily assignable to the two crystal forms of **4** present in

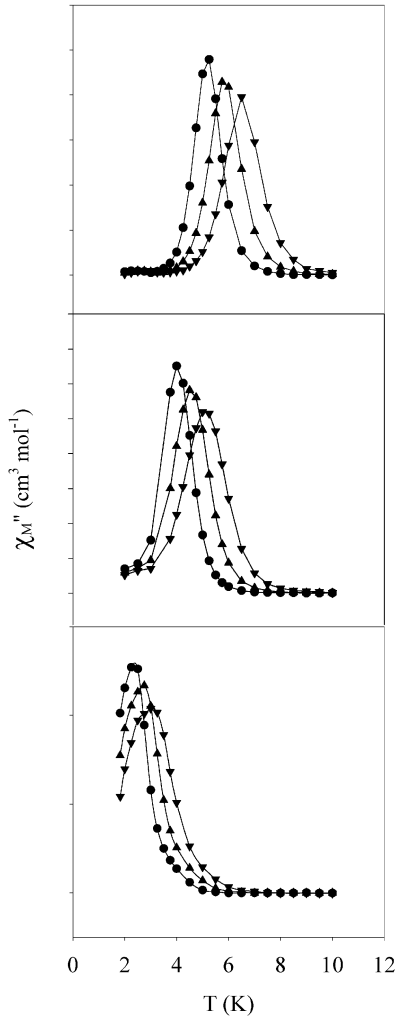

Figure 9. χ_M'' vs T plots for Mn_{12} complex **2** (top), $[Mn_{12}]^-$ complex **3** (middle), and $[Mn_{12}]^{2-}$ complex **4** (bottom) at 1000 (▼), 250 (▲) and 50 Hz (●).

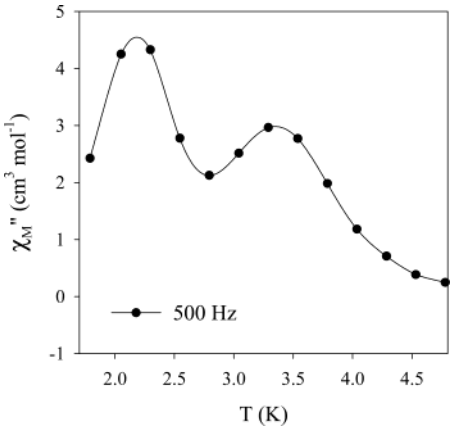

Figure 10. χ_M'' vs T plot for a wet crystalline sample of complex **4** at 500 Hz.

crystalline samples. Subsequent studies using hand-picked plates of **4**·4CH_2Cl_2·H_2O (**4a**) gave only the lower-temperature signal, and the higher-temperature signal is thus due to **4**·6CH_2Cl_2 (**4b**). Bulk samples (not hand-picked) vary in their relative content of **4a** and **4b** and thus give a variation in the relative ratio of the two χ_M'' signals; in some cases, the higher-temperature signal is barely visible. Resolution of the two peaks is only seen with

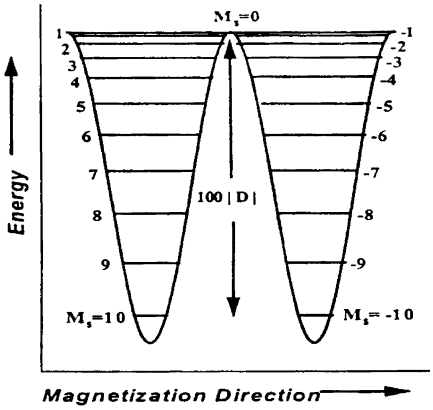

Figure 11. Double-well potential energy plot for an $S = 10$ molecule with axial symmetry and easy-axis type anisotropy. The energy separation between the $M_s = \pm 10$ and $M_s = 0$ orientations of the magnetization is given by $S^2|D|$.

crystals kept wet with mother liquor; removal of the mother liquor initiates solvent loss, and the peaks get progressively broader with time and merge into one broad peak.

Relaxation Studies Using AC and DC Data. The χ_M'' vs T plots were used as a source of kinetic data to calculate the effective energy barrier (U_{eff}) to magnetization relaxation. At a given oscillation frequency (ν), the position of the χ_M'' peak maximum is the temperature at which the angular frequency ($\omega = 2\pi\nu$) of the oscillating field equals the relaxation rate ($1/\tau$, where τ is the relaxation time) at which a molecule relaxes between the halves of the double-well potential energy plot (Figure 11). The relaxation rates at a given temperature can thus be obtained from $\omega = 1/\tau$ at the maxima of the χ_M'' peaks. For single or resolved pairs of peaks, the peak maxima were accurately determined by fitting the peaks to a Lorentzian function; for broad peaks from two unresolved signals, the peak maxima were visually determined.

The magnetization relaxation of a SMM obeys the Arrhenius relationship (eq 4),

$$(1/\tau) = (1/\tau_0)\exp(-U_{eff}/kT) \quad (4a)$$

$$\ln(1/\tau) = \ln(1/\tau_0) - U_{eff}/kT \quad (4b)$$

the characteristic behavior of a thermally activated Orbach process, where U_{eff} is the effective anisotropy energy barrier and k is the Boltzmann constant.

For crystalline samples of complex **4** comprising **4a** and **4b**, the frequency-dependence of both sets of χ_M'' peaks was determined at eight different oscillation frequencies in the 5−1500 Hz range. For the lower-temperature peaks, only at the four highest frequencies were the peak maxima observed at 1.8 K or above, the limit of our instrument. Thus, it was felt that not enough data over a sufficiently large frequency and temperature range were available for an accurate kinetic analysis. The AC data were therefore supplemented with relaxation data to lower temperatures determined from DC relaxation decay measurements on single crystals of **4a** (and **4b** also) using a micro-SQUID apparatus. First, a large DC field of 1.4 T was applied to the sample at about 5 K to saturate its magnetization in one direction, and the temperature was then lowered to a chosen value between 0.04 and 2 K. When the temperature was stable, the field was swept from 1.4 to 0 T at a rate of 0.14 T/s,

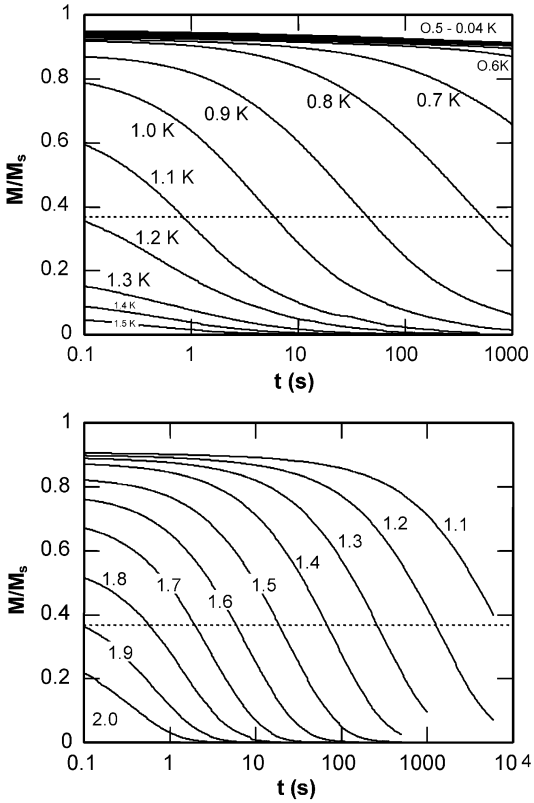

Figure 12. Magnetization vs time decay plots in zero field for (top) complex **4a** (plates), and (bottom) complex **4b** (needles). The magnetization is normalized to its saturation value M_s, and the dashed line indicates the $M/M_s = 1/e$ point.

and then the magnetization in zero field was measured as a function of time. The results are shown in Figure 12, with the magnetization normalized to its saturation value M_s. The relaxation time (τ) at each temperature was obtained by calculating the time required for M/M_s to fall to a value of $1/e$, as expected for exponential decay (dashed lines in Figure 12). This is exactly true for SMMs where every molecule is identical with identical barriers; in practice, samples of SMMs contain a (relatively small) range of barriers, due to small environmental differences such as ligand or solvent disorder, solvent loss, crystal defects, and so forth, and the above method of obtaining τ is an approximation, but a very reasonable one.

The combined AC and DC data were fit to eq 4; the data and the fits (solid lines) are plotted as τ vs $1/T$ in Figure 13. For platelike complex **4a**, $U_{eff} = 18.5$ K and the preexponential factor is $1/\tau_o = 1.9 \times 10^7$ s^{-1}. For needlelike complex **4b**, $U_{eff} = 30.3$ K and the preexponential factor is $1/\tau_o = 3.1 \times 10^7$ s^{-1}. These correspond to the lower- and higher-temperature peaks of Figure 10, respectively. Thus, the two crystalline forms of complex **4** have significantly different barriers to magnetization relaxation, differing by almost a factor of 2.

The χ_M'' vs T data for dried complex **4** were analyzed similarly using only the AC data (the micro-SQUID technique requires single crystals), and the results are shown in Figure 14. The obtained values were $U_{eff} = 32$ K and $1/\tau_o = 3.1 \times 10^8$ s^{-1}. The U_{eff} and $1/\tau_0$ values obtained for this dried $[Mn_{12}]^{2-}$ complex can be compared with those obtained from AC χ_M'' vs frequency studies for dried samples of the Mn_{12} (**2**) and $[Mn_{12}]^-$ (**3**) analogues, whose data are also shown in Figure 14. The corresponding values are $U_{eff} = 66$ K and $1/\tau_o = 2.0$

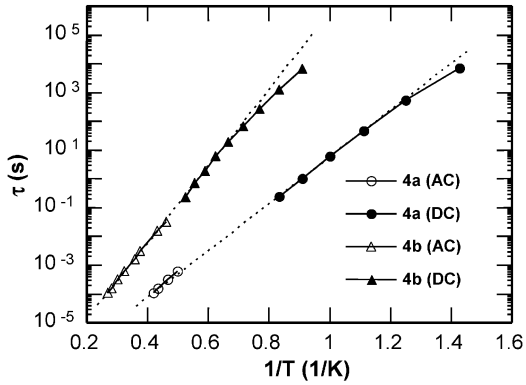

Figure 13. Plots of relaxation time (τ) vs. $1/T$ for complexes **4a** and **4b** using AC χ_M'' and DC decay data. The solid lines are fits to the Arrhenius equation. See Table 6 for the fitting parameters.

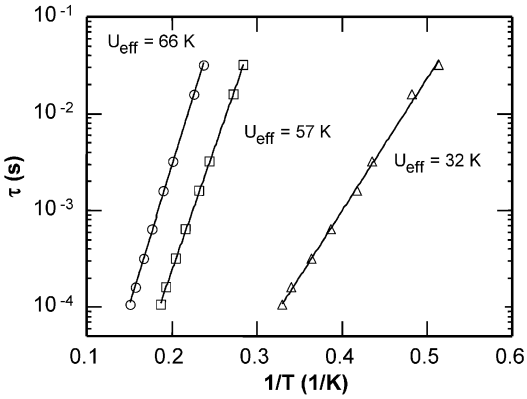

Figure 14. Plots of relaxation time (τ) vs $1/T$ for dried complexes **2** (○), **3** (□), and **4** (△) using AC χ_M'' data. The solid lines are fits to the Arrhenius equation. See Table 6 for the fit parameters.

Table 6. Arrhenius Data for $[Mn_{12}O_{12}(O_2CCHCl_2)_{16}(H_2O)_4]^{0,-,2-}$ Complexes

	dried samples			wet crystals	
parameter	$z = 0$ (**2**)	$z = 1-$ (**3**)	$z = 2-$ (**4**)	$z = 2-$ (**4a**)	$z = 2-$ (**4b**)
spin	10	19/2	10	10	10
range, K[a]	6−8	4−6	2−4	2−3	3−4
U_{eff}, K[b]	66	57	32	18.5	30.3
$1/\tau_o$, s^{-1} [b]	2.0×10^8	5.8×10^8	3.1×10^8	1.9×10^7	3.1×10^7

[a] Temperature range of χ_M'' peaks. [b] From Arrhenius plot.

$\times 10^8$ s^{-1} for Mn_{12} (**2**) and $U_{eff} = 57$ K and $1/\tau_o = 5.8 \times 10^8$ s^{-1} for $[Mn_{12}]^-$ (**3**) (Table 6). The U_{eff} values decrease on reduction, as expected from the decreasing Mn^{III} content mentioned earlier. The trend is monotonic but not linear, and this is as expected: the U_{eff} value depends not just on S and D but also on the rhombic ZFS parameter E, fourth-order spin Hamiltonian parameters, the precise tunneling channel of the QTM (i.e., which M_s levels are involved), and other parameters. These depend on many factors, including the site-symmetry of the complex, and, for example, the $[Mn_{12}]^{z-}$ complexes do not all crystallize in the same space group. Thus, there are too many parameters that contribute to the observed U_{eff} to permit a quantitative comparison between different complexes.

Hysteresis Loops. The conclusion that the various forms of complex **4** all have a significant barrier to magnetization relaxation suggested that hysteresis loops should be observed. Hysteresis in magnetization vs DC field sweeps is the classical property of a magnetic material. The studies were performed

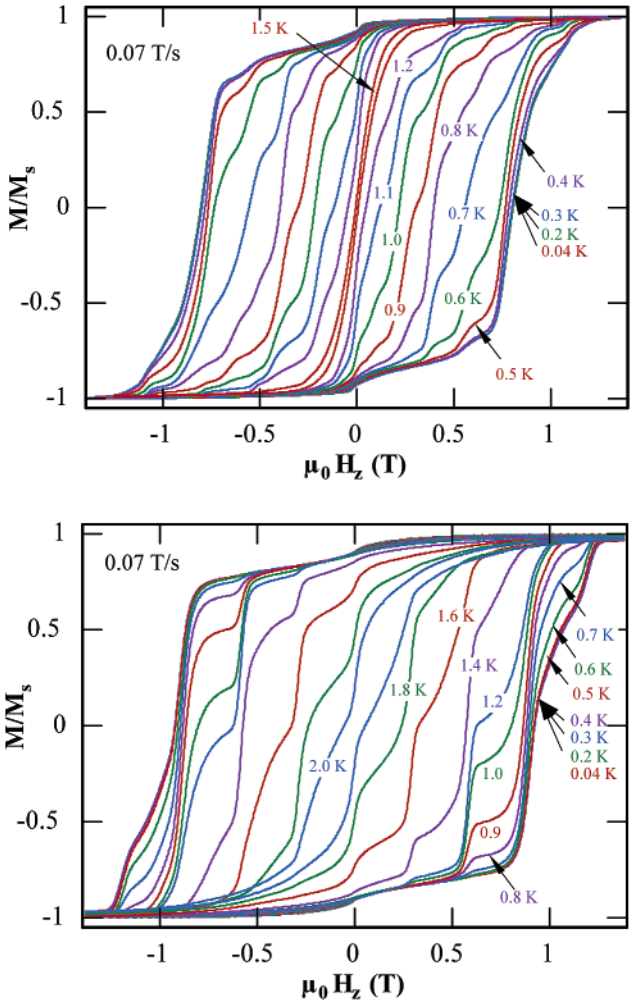

Figure 15. Magnetization hysteresis loop for complex **4a** in the 0.04−1.5 K temperature range at a 0.07 T/s field sweep rate (top). Magnetization hysteresis loop for complex **4b** in the 0.04−2.0 K range at 0.07 T/s sweep rate (bottom).

on aligned single crystals of **4a** and **4b** using a micro-SQUID apparatus, and the resulting hysteresis loops at temperatures <2 K and a 0.07 T/s sweep rate are shown in Figure 15. Both **4a** and **4b** display clear hysteresis with coercivities that vary with temperature, as expected for SMMs, becoming temperature-independent only at very low temperatures (0.3 and 0.4 K for **4a** and **4b**, respectively) where crossover occurs to pure ground state tunneling, i.e. thermally activated relaxation ceases and there is tunneling only from the lowest-lying $M_s = -10$ level. Since this crossover T is proportional to S and D, this implies that D for **4a** is less than that for **4b**.

The hysteresis loops are not smooth but instead comprise plateaulike regions separated by steps that represent positions of increased relaxation rate and which are the signature of quantum tunneling of magnetization (QTM). The steps occur at periodic values of applied magnetic field whenever an M_s level on one side of the potential energy double well is in resonance with an M_s' level on the other side, such as in zero applied field where the double well is symmetric (Figure 11) and in applied fields where the double well is asymmetric. The field separation between steps (ΔH), which can best be determined from the first derivative of the hysteresis loop, is

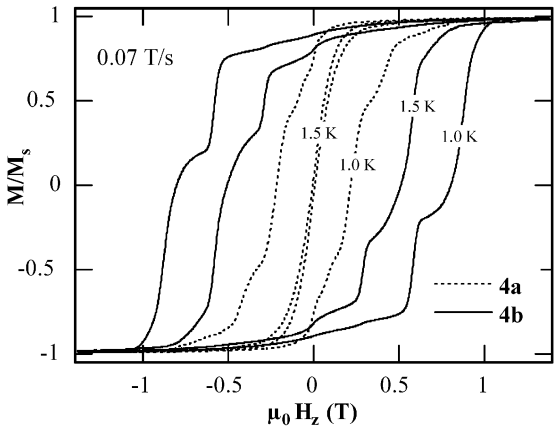

Figure 16. Comparison of the hysteresis loops at 1.0 and 1.5 K for complexes **4a** and **4b** at a 0.07 T/s sweep rate.

proportional to D and is given by eq 5.

$$\Delta H = \frac{|D|}{g\mu_B} \tag{5}$$

Measurement of the step positions in Figure 15 gave an average ΔH of 0.186 T (1.86 kG) for complex **4a** and 0.300 T (3.00 kG) for complex **4b**. These correspond to $|D|/g$ values of 0.087 and 0.14 cm^{-1} for **4a** and **4b**, respectively, and again indicate that the $|D|$ value for **4a** is smaller than that for **4b**, since the g values are expected to be very similar, if not identical.

A close comparison of the two halves of Figure 15 shows that at the same sweep rate and temperature, the coercivity of the hysteresis loop of **4a** is much smaller than that of **4b**. This is shown more clearly in Figure 16, which compares the loops at 0.07 T/s for the two complexes at 1.0 and 1.5 K. This rather dramatic difference is again a consequence of the lower barrier to magnetization relaxation for **4a** vs **4b**, as quantitated from the Arrhenius plots.

Discussion

The ability to exchange the acetate groups of complex **1** with any other carboxylate of choice using the ligand substitution methods developed earlier has allowed us to fine-tune the redox potentials of these Mn_{12} species. The use of strongly withdrawing substituents has raised the reduction potentials to the point that the second reduction is now within the capability of our reductant of choice, iodide I^-, and clean, two-electron reduction to $[Mn_{12}]^{2-}$ salts has successfully been carried out. The products are stable and have been isolated for the $Cl_2CHCO_2^-$ derivative.

The structural characterization establishes that the added electrons are localized on formerly Mn^{III} sites to give a trapped-valence $2Mn^{II}$, $6Mn^{III}$, $4Mn^{IV}$ situation, with the Mn^{II} sites being disposed trans within the $[Mn_{12}O_{12}]$ core. This trapped-valence situation persists in the solid state at room temperature and can be assigned to the Jahn−Teller distortion at each Mn^{III} site, resulting in significant barriers to electron de-trapping. Trapped valency is, almost without exception, the observed situation in mixed-valence Mn^{II}/Mn^{III}, Mn^{III}/Mn^{IV}, and $Mn^{II}/Mn^{III}/Mn^{IV}$ complexes. In solution, however, on the ^1H NMR time scale, the spectra are consistent with effective D_{2d} symmetry, which can be assigned to electron de-trapping that is fast (on this time scale) and likely facilitated by a previously identified fluxional process involving one type of the axial carboxylate ligands and bound H_2O groups. The NMR spectra also confirm the structural integrity of the $[Mn_{12}]^{2-}$ complexes in solution, at least in chlorinated hydrocarbons. True solubility, as opposed to colloidal suspension, is a major advantage of SMMs over classical magnetic particles.

Given that the Mn_{12} and $[Mn_{12}]^-$ species are SMMs, the magnetic properties of the $[Mn_{12}]^{2-}$ derivatives were of particular interest, and magnetization studies established that the latter retain both a large ground-state spin value of $S = 10$, identical to the neutral Mn_{12} species, and a significant easy-axis type (Ising type) magnetoanisotropy, as reflected in the magnitude and sign of the axial zero-field splitting parameter, D. The absolute magnitude of the latter is, however, smaller than those of the Mn_{12} and $[Mn_{12}]^-$ species, and this is consistent with a decreasing Mn^{III} content on reduction, these ions being the major source of the molecular magnetoanisotropy. As a result, the barrier to magnetization relaxation for the $[Mn_{12}]^{2-}$ complexes, which is proportional to S and D, is smaller than those of the Mn_{12} and $[Mn_{12}]^-$ complexes, and thus the latter two species are SMMs at higher temperatures than $[Mn_{12}]^{2-}$. This is due to the changing D value, since the S values are essentially constant at $S = 10$, $^{19}/_2$, and 10 for the Mn_{12}, $[Mn_{12}]^-$, and $[Mn_{12}]^{2-}$ complexes, respectively. In this regard, it would have been of interest had the added electrons become localized on the central cubane Mn atoms, converting them from Mn^{IV} to Mn^{III}; this might have maintained a high D value, but of course it might also have led to a smaller S value as the strong antiferromagnetic coupling between the inner Mn^{IV} and outer Mn^{III} ions responsible for the high S value became weaker.

Despite their decreased D values, the $[Mn_{12}]^{2-}$ complexes are still SMMs and display both out-of-phase AC susceptibility signals and the classical property of a magnet, namely magnetization hysteresis. However, it is clear that the two crystal forms of complex **4**, namely **4a** and **4b**, have distinctly different properties. Complex **4a** has a significantly smaller barrier, U_{eff}, than **4b**, and consequently a lower blocking temperature (T_B) of 1.5 K compared with that for **4b**, which is slightly above 2 K. In fact, we had originally thought this might be due to Jahn−Teller isomerism, in which one (or more) of the Mn^{III} JT elongation axes are abnormally oriented equatorially with respect to the $[Mn_{12}O_{12}]$ core instead of the usual axial.[18] This phenomenon was first identified in faster-relaxing, neutral Mn_{12} complexes and results in U_{eff} values only approximately 50−60% the magnitude of those in normal Mn_{12} complexes. However, close examination of the crystal structures of **4a** and **4b** shows that all Mn^{III} JT axes are in normal orientations. Thus, the difference in U_{eff} values in this case is not JT isomerism, and it must instead be assigned to the differing space groups of the two crystal forms and the resulting slightly different site-symmetries and environments of the $[Mn_{12}]^{2-}$ species in the two crystals. But these differences are very small: in both cases, the cations are PPh_4^+, the relative packing of anions and cations in the two structures is not that different (see Supporting Information), and the solvent content is similar, $4CH_2Cl_2 \cdot H_2O$ in **4a**, and $6CH_2Cl_2$ in **4b**. The lattice H_2O molecule of the

(18) (a) Sun, Z.; Ruiz, D.; Rumberger, E.; Incarvito, C. D.; Folting, K.; Rheingold, A. L.; Christou, G.; Hendrickson, D. N. *Inorg. Chem.* **1998**, *37*, 4758. (b) Sun, Z.; Ruiz, D.; Dilley, N. R.; Soler, M.; Ribas, J.; Folting, K.; Maple, M. B.; Christou, G.; Hendrickson, D. N. *Chem. Commun.* **1999**, 1973. (c) Aubin, M. J.; Sun, Z.; Eppley, H. J.; Rumberger, E. M.; Guzei, I. A.; Folting, K.; Gantzel, P. K.; Rheingold, A. L.; Christou, G.; Hendrickson, D. N. *Polyhedron* **2001**, *20*, 1139.

former is involved in hydrogen-bonding with a bound H_2O ligand on the $[Mn_{12}]^{2-}$ anion (O19···O100 = 2.618 Å) but does not bridge to a neighboring one. Thus, the two crystals have different space group symmetries and their $[Mn_{12}]^{2-}$ units are indeed in different environments, but these differences are small. It is consequently surprising that the calculated U_{eff} values and resulting hysteresis loops are so different, relatively speaking. Had the two crystals forms involved very different cations and much different solvent content, these differences would still have been significant, but at least they would be less surprising.

Even though the environments and separations of the $[Mn_{12}]^{2-}$ ions in **4a** and **4b** are similar, they are not identical, and differences in their site-symmetries will likely be reflected in differences in their transverse (rhombic) anisotropy parameter, *E*. The tunneling rates are strongly dependent on the latter. Thus, a lowering of symmetry will lower *D* and increase *E*, and thus increase the relaxation rate at a given temperature. This is consistent with the observation that **4a** has a smaller *D* and smaller U_{eff} than **4b**. It will require other studies, such as single-crystal high-frequency EPR, to obtain accurate values of *E* for **4a** and **4b** and permit more quantitative considerations.

Ultimately, the differences between **4a** and **4b** are dependent on the solvent molecules in the lattice, because when crystals of **4a** and **4b** are removed from mother liquor and lose solvent, their AC χ_M'' peaks broaden and merge, and a U_{eff} similar to that of **4b** results. This suggests it is the low U_{eff} of **4a** (18.5 K) that is unusual, and it will be interesting in the future to compare with the U_{eff} values of other $[Mn_{12}]^{2-}$ complexes that are being made and studied. It is clear that a larger database of crystal structures and associated U_{eff} determinations will be needed before a better understanding of the origin of the differences between **4a** and **4b** is attained. However, the conclusion from the present work is clearly that the properties of SMMs are very sensitive to, and are significantly modified by, environmental influences even in the absence of clear intramolecular structural perturbations such as JT isomerism.

Complexes **4a** and **4b** exhibit steps on their hysteresis loops that are the diagnostic signature of quantum tunneling of magnetization (QTM), as previously demonstrated for both the Mn_{12} and $[Mn_{12}]^-$ complexes. Thus, all three isolated oxidation levels of the Mn_{12} family display this important quantum behavior, providing a useful expansion to the database. In fact, analysis of the step separation is a useful indicator of the *D* values of **4a** and **4b**; actually, it gives *D*/*g*, but the *g* values can safely be assumed to be very similar at $g \approx 2$. A $g = 2$ value gives $D = -0.17$ and -0.28 cm^{-1} for **4a** and **4b**, independently confirming that the subtle combination of environmental differences between the two structures is causing a noticeable difference in the magnitude of *D* and that the latter is thus the main source of the differences in U_{eff}. Note that dried **4** is no longer crystalline and cannot be studied using the micro-SQUID apparatus to obtain *D*/*g* from the hysteresis loops. Nevertheless, its $|D|/g$ is available from the bulk magnetization data which gave 0.14 ± 0.01 cm^{-1}. This is the same as the $|D|/g = 0.14$ cm^{-1} for **4b**, again consistent with **4a** being the unusual form of complex **4** with respect to magnetic properties.

It should be noted that the $[Mn_{12}]^{2-}$ complexes have recently also been demonstrated[19] to exhibit another important quantum behavior, namely quantum phase interference.[20] This is one of the most interesting quantum phenomena that can be studied at the mesoscopic level in SMMs, and had been previously observed only for the Fe_8 SMM.[21] The sample used was complex **4b**, which is thus the second SMM to clearly show this effect. The studies involved using the Landau−Zener method[22] in the thermally activated regime to measure the tunneling rate as a function of transverse field applied along the hard anisotropy axis. Oscillations of the tunnel probability as a function of field were observed, which are due to topological quantum interference of two tunnel paths of opposite winding.[19] The period of oscillation allowed a useful preliminary estimation of the rhombic anisotropy constant *E* for **4b** of ∼0.04 cm^{-1} (∼0.06 K).

Conclusions

A third oxidation level of the Mn_{12} family of SMMs has been successfully isolated and studied. Complex **4** has been obtained in two crystal forms, both of which have been structurally characterized. They both have normal orientations of their JT axes, but there are distinct differences in their magnetic properties, which can be assigned to different $[Mn_{12}]^{2-}$ site-symmetries due to the environmental differences about the $[Mn_{12}]^{2-}$ anions resulting from the different space groups of the two forms. AC and DC susceptibility studies establish they have $S = 10$ but distinctly different U_{eff} values that arise primarily from different values of the axial anisotropy parameter *D*. This again emphasizes the importance of the environment and local symmetry about a SMM on the resulting magnetic properties. Both **4a** and **4b** display resonant QTM as do the Mn_{12} and $[Mn_{12}]^-$ analogues, and the present work thus provides another useful integer-spin system with which to study this important quantum behavior, as well as quantum phase interference.

In future reports, we shall describe the syntheses, structures, and properties of several more $[Mn_{12}]^{2-}$ complexes that are currently in progress, as well as the results of our attempts to isolate three-electron reduced complexes and one-electron oxidized ones.

Acknowledgment. This work was supported by the National Science Foundation.

Supporting Information Available: X-ray crystallographic files in CIF format for complexes **4**·4CH_2Cl_2·H_2O (**4a**) and **4**·6CH_2Cl_2 (**4b**). Unit cell packing diagrams for the two structures (Figures S1 and S2), the $\chi_M T$ vs *T* plot for dried complex **4** (Figure S3), and a table comparing the structural parameters from the crystal structure of complex **4a** at −80 and +22 °C (Table S1) (PDF). This material is available free of charge via the Internet at http://pubs.acs.org.

JA021066S

(19) Wernsdorfer, W.; Soler, M.; Christou, G.; Hendrickson, D. N. *J. Appl. Phys.* **2002**, *91*, 7164.
(20) Garg, A. *Europhys. Lett.* **1993**, *22*, 205.
(21) Wernsdorfer, W.; Sessoli, R. *Science* **1999**, *284*, 133.
(22) Wernsdorfer, W.; Sessoli, R.; Gatteschi, D. *Europhys. Lett.* **1999**, *47*, 254.